doi:10.1038/nature12155

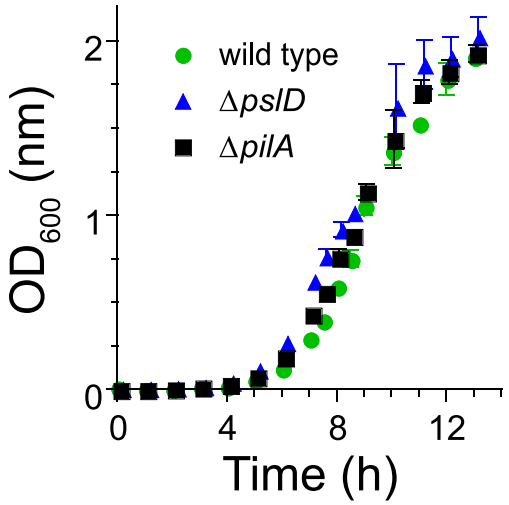

Supplementary Figure 1. Growth rates of strains used in this study. The OD_{600} of planktonic cells growing in FAB containing 30 mM glutamate was measured for 14 hours. WT, green circles; Δ*pslD*, blue triangles; Δ*pilA*, black squares. Error bars represent standard deviation of three experiments. Results show that the growth rates are essentially identical.

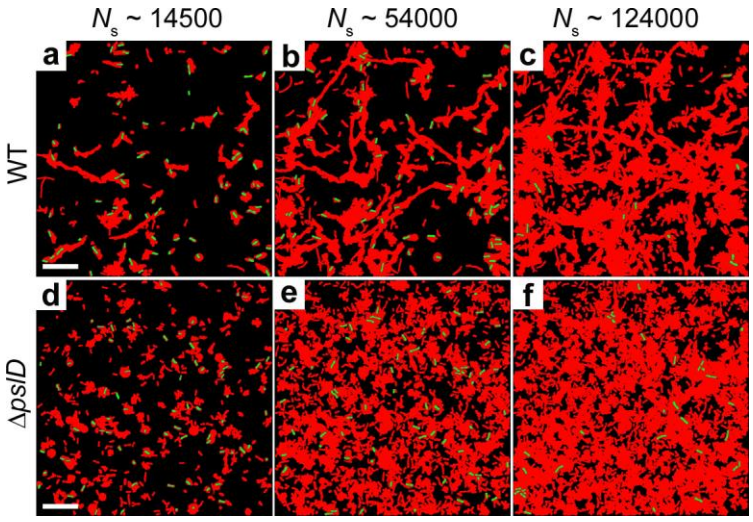

Supplementary Figure 2. Efficiency of surface coverage by bacterial trajectories, compared for the same total number of bacterial visits for each strain rather than for the same time. Data for WT and Δ*pslD* are compared at the same total number of bacterial visits, i.e. for the same $N_s = \Sigma n_i$, where n_i is the number of bacteria in frame i. $N_s \sim 14{,}500$ for panels (**a**, **d**), $N_s \sim 54{,}000$ for panels (**b**, **e**) and $N_s \sim 124{,}000$ for panels (**c**, **f**). Top row is for WT and bottom row is for Δ*pslD*. Red and black regions indicate cell-traversed or used surfaces (i.e. surfaces that have been covered by bacterial trajectories) and fresh surfaces, respectively. Bacteria in the current frame are shown in green. Scale bars are 10 μm.

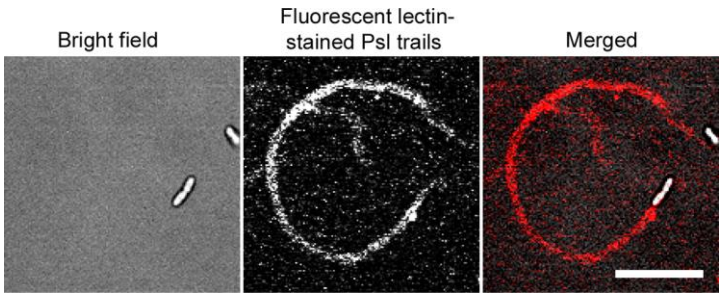

Supplementary Figure 3. Psl trail left behind by bacteria. Left, Brightfield image of the bacteria. Center, Psl trail stained by fluorescently conjugated HHA lectin. Right, merged image with trail pseudo-colored in red. Scale bar is 10 μm.

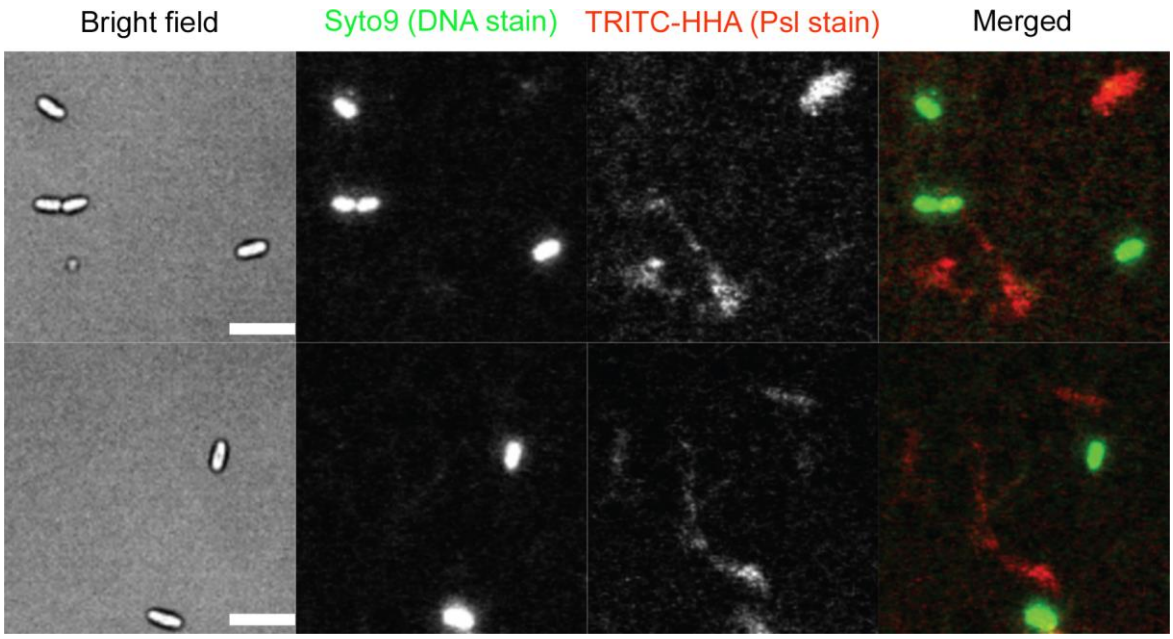

Supplementary Figure 4. Co-staining of surfaces with TRITC-HHA and Syto9. Syto9 staining shows no DNA outside of the cells, while TRITC-HHA lectin staining shows the Psl trails left by bacteria. The merged image of Syto9 staining and TRITC-HHA staining confirms that eDNA is not co-localized with Psl trails, suggesting that eDNA does not constitute a major component of the Psl trails at this stage of biofilm development. Two representative image sets are shown (top row and bottom row). The experiment was repeated three times with ≥ 10 images acquired per experiment. Scale bars are 5 μm.

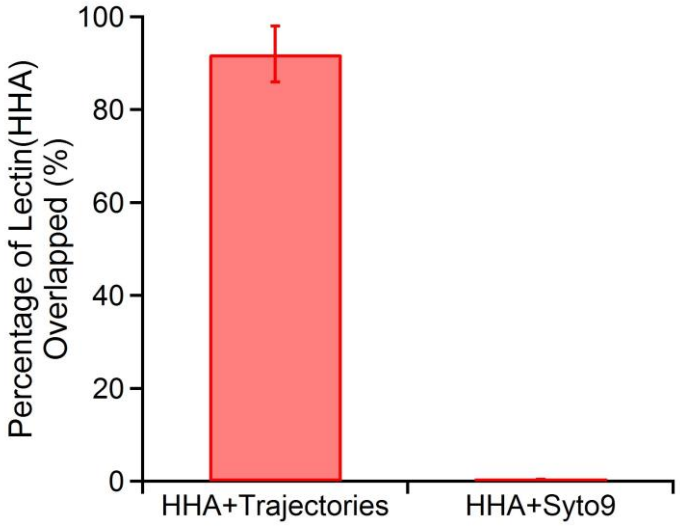

Supplementary Figure 5. Regions of HHA lectin staining co-localize with the tracked bacterial trajectories but not with Syto9. Using the data sets presented in the paper, the regions stained with the HHA lectin were analyzed for co-localization with the tracked trajectories (left) or Syto9 (right). Error bars represent standard deviation of three experiments.

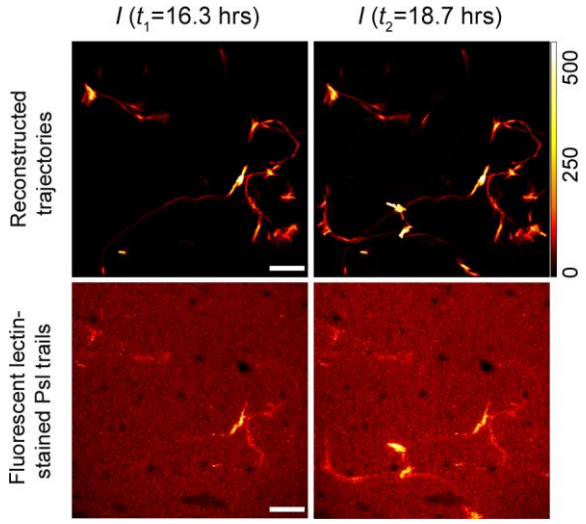

Supplementary Figure 6. Correlation between trajectories and Psl trails. Reconstructed trajectories (top row) and fluorescent lectin-stained Psl trails (bottom row) up to time points t_1 (16.3 hours after inoculation) and t_2 (18.7 hours after inoculation). Scale bars are 10 μm. Color bar indicates the time a given cell spent at each point (in the unit of number of bacterial visits).

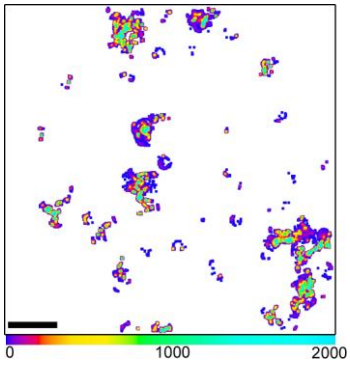

Supplementary Figure 7. Visit frequency distribution of Δ*pilA*. Color-coded visit frequency map of Δ*pilA* for the first 10 hours shows completely different behavior compared to WT (Figure 2a, main text), with little surface exploration. The hierarchical web of trajectories exhibited by WT is no longer observed. Scale bar is 10 μm.

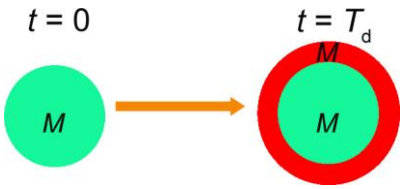

Supplementary Figure 8. Schematic graph showing how exponential growth within immobile microcolonies leads to exponential visit frequency distributions. To see why the development of immobile microcolonies leads to an exponential visit distribution, we consider a simple approximate model with synchronized divisions. At time $t = 0$, an early microcolony with M cells resides on a circular patch of the surface (denoted by light green filled circle on left). For relatively immobile bacteria, the number of bacterial visits is essentially the cell residence time on a surface. We assume that all divided daughter cells form an immobile monolayer with an average cell density that does not change significantly with additional division cycles. After a total elapsed time of i doubling times $t = i\,T_d$, there are $i+1$ generations, with the j^{th} generation ($1 \le j \le i$) containing $2^{j-1}M$ cells (generation $j = 0$ contains M cells, evidently). For a sampling interval T_s the j^{th} generation will yield $((i+1-j)\,T_d / T_s) = (m\,T_d / T_s)$ visits per cell, so that the visit frequency, parameterized by $m = i+1-j$, is proportional to

$$\begin{cases} 2^{(i-m)}M & \text{for } 1 \le m \le i \\ M & \text{for } m = i+1 \\ 0 & \text{for } m > i+1 \end{cases}$$

This visit distribution decreases exponentially with increasing m. The assumptions in this simple model are expected to hold for initial stages of PAO1 early microcolony formation, but will break down as more complex three-dimensional growth occurs.

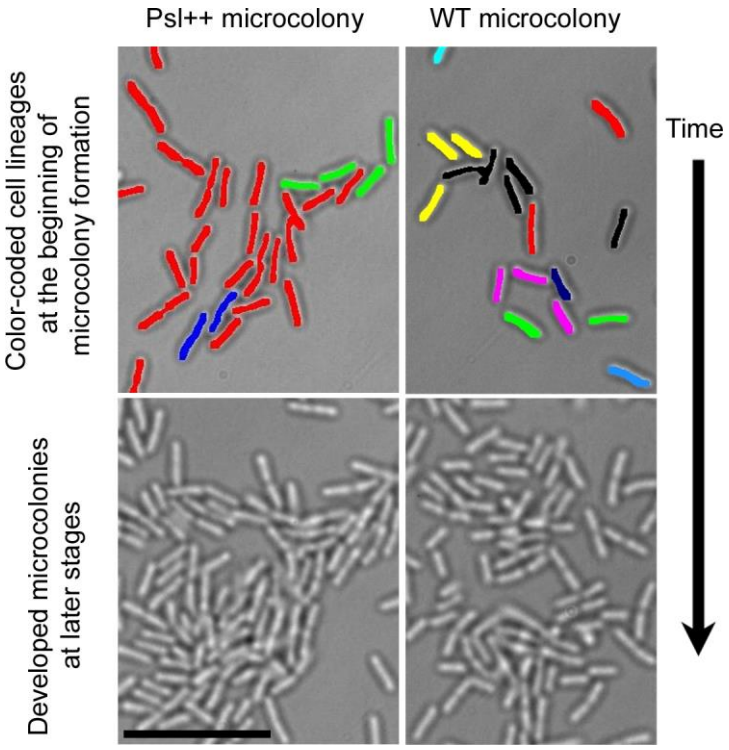

Supplementary Figure 9. Additional examples of cell lineages for microcolonies. WT and Psl++ microcolonies have drastically different compositions of lineages. The top row depicts the color-coded cell division lineages at early stages of microcolony formation and the bottom row shows more developed microcolonies at the same location 3.3 hours later. The color coding distinguishes cells depending on whether they are related by division, so that different lineages of cells within the microcolony (present due to motile cells joining the microcolony, cells attaching from solution, etc.) are depicted by different colors. The scale bar is 10 μm.

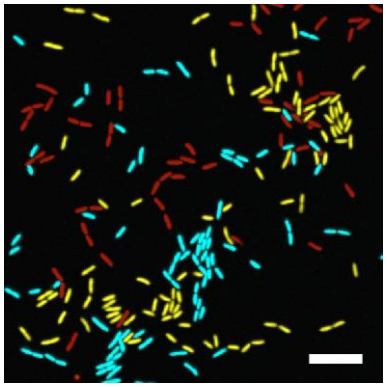

Supplementary Figure 10. Clusters of differentially labeled WT cells. A flow cell was seeded with equal numbers of three differentially labeled WT PAO1 cell lines (pseudo-colored red, yellow and cyan in the micrograph) and grown under flow in FAB containing 0.6 mM glutamate until clusters formed. Images were acquired using confocal microscopy. These results show that WT microcolonies are composed of different cell lineages (colors), consistent with our tracking results. The scale bar is 10 μm.

Supplementary Methods

Repetition of experiments for specific conditions

For a given set of conditions our observations are based inherently on a large number of microscopic repeats. However, this does not account for run-to-run variations. Our tracking experiments for each set of conditions were repeated a minimum of three times. Due to inevitable small variations in inoculation density and other experimental parameters, the timing of the first bacterial attachment event in the field of view is effectively random, so that measurements for different runs cannot be averaged directly. In the main manuscript, we presented results for one representative data set and propagated estimated measurement error. Here we show that the run-to-run variations between separate experiments are small compared to the observed differences between WT and the Δ*pslD* mutant. More important, we show why such run-to-run variations do not affect the measured power laws that govern how the bacteria self-organize on the surface.

There is inherent unpredictability in when bacteria will attach to a surface, as observed in flow cell experiments. Each bacterium has a different set of initial conditions (position, velocity, physiological state, etc.); therefore, it cannot be predicted when a bacterium will encounter a surface or how many surface encounters are required before it can successfully attach. However, once bacteria attach to a surface and start exploration, they will systematically organize in a manner described by the measured power laws, with very little uncertainty in the exponent of the power law. The errors in the measured exponents of the power laws are quite small (≤ 0.1) *even* for data sets that display the largest run-to-run variations in the corresponding surface coverage plots. The reason is that run-to-run variations in the surface coverage plots reflect mostly the

stochastic differences in when bacteria start to colonize a surface. For example, an experiment in which cells stochastically attach to the surface earlier will get a head start and therefore cover a larger percentage of the surface. However, even though these cells start earlier, they still follow the same rules stringently, i.e. the same power-law visit distributions, with almost no leeway in the exponents.

In the case of surface coverage, the comparison of corresponding time points for different runs with different strains may be affected by variations in cell number. To test whether such variations make a difference, we normalized our data using the cumulative number of bacterial visits N_s. At N_s = 124,000, the surface coverage of the WT was 52 ± 4% (average ± SEM; N=5), whereas that of the Δ*pslD* mutant was 83 ± 10% (average ± SEM; N=3). We also calculated the P-value from a Mann-Whitney U-test, which is 0.036 (two-tailed test). Therefore, the surface coverages of WT and Δ*pslD* are statistically different. Differences in the power-law slopes for the visit frequency distributions are stringent tests due to their logarithmic nature, as large changes in the motility patterns are necessary to observe significant changes in the exponents of the power law. The slopes for three replicates (WT) were –2.9, –3.0 and –2.83, resulting in an average of –2.9 ± 0.1 (SD). Similarly the exponents for three repeats of $\Delta P_{psl}/P_{BAD}$-*psl* strain are –3.3, –3.2 and –3.3 at 0% arabinose concentration, –2.4, –2.4 and –2.5 at 0.1% arabinose concentration and –1.9, –1.9 and –1.9 at 1% arabinose concentration. Thus, the variation in the exponent from run to run is estimated to be within 0.1. This uncertainty is significantly smaller than the variation of exponents we observe with changing arabinose concentrations (–3.3 to –1.9).

Cells that stay only transiently on the surface can affect surface exploration in complex ways. Excluding them would imply that we ignore their potential Psl production. However, including them might affect the statistics of surface exploration. To see how inclusion of short

visits affect the surface coverage, we repeat the same analysis we performed for Figure 1a-d, but leave out those bacteria with residence times shorter than 9 seconds. As shown in Supplementary Figure 11, when all bacteria were included in the analysis ($t_{res} > 0$ s), the surface coverages for WT and Δ*pslD* were 52 ± 4% and 83 ± 10% at N_s = 124,000, respectively (Supplementary Figure 11a). If only bacteria with residence times greater than 9 seconds were included ($t_{res} > 9$ s), the corresponding surface coverages changed to 48 ± 4% (WT) and 74 ± 13% (Δ*pslD*) (Supplementary Figure 11b). When short visits are omitted, the surface coverage will systematically decrease for both strains. However, the trend that Δ*pslD* mutants cover the surface more efficiently than WT persists, and the ratio of surface coverages between Δ*pslD* and WT only changes from $R_{>0}$ = 1.60 to $R_{>9}$ = 1.54. Importantly, since the data set is inherently spatiotemporal rather than just spatial in nature, the most stringent test is the set of power laws we observe. The difference in the power-law slopes for the visit frequency distributions between data sets of $t_{res} > 0$ s and $t_{res} > 9$ s is negligible (the slopes are the same within fitting error). In fact, it can be seen that the omission of transiently attached cells affects mostly the first data point in the power-law visit distributions.

Division and post-division cell fates

We determined the division events by searching for cases where one mother cell in frame *i* became two daughter cells in frame *i*+1. Each daughter cell was assigned a new identification number, which can be used to construct a pedigree chart. Typically, hundreds of division events were detected per run under the specified experimental conditions. In our analysis of post-division motility behavior, we defined the states of post-division cells as follows: A post-division cell is defined as one that *stays* if the cell's next division event is still detected in the field of view. By contrast, a post-division cell is defined as one that *leaves* the vicinity of the

division event if its next division is not detected in the field of view either due to surface motility or to cell detachment. This is similar to the definitions used in reference 33.

Bacterial strains and growth conditions for strain construction

Bacterial strains used in this study are listed in Supplementary Table 1. *P. aeruginosa* was grown at 37 °C in lysogeny broth (LB, 10 g l^{-1} tryptone, 5 g l^{-1} yeast extract, 5 g l^{-1} NaCl) or in Vogel–Bonner minimal medium (VBMM; 0.2 g 1^{-1} $MgSO_4$•$7H_2O$, 2.0 g 1^{-1} citric acid, 3.5 g 1^{-1} $NaNH_4HPO_4$•$4H_2O$, 10 g 1^{-1} K_2HPO_4, pH 7.0)[34]. Semi-solid media were prepared by adding 1.5% Bacto agar to LB or 1.0% noble agar to VBMM. *Escherichia coli* strains were routinely cultured using LB media. Antibiotics were added to maintain or select for plasmids as follows: for *E. coli*, gentamicin (Gm) at 10 μg/ml, spectinomycin (Sp) at 50 μg/ml, kanamycin (Km) at 50 μg/ml; for *P. aeruginosa*, Gm at 100 μg/ml for plasmid-borne strains and 30 μg/ml for chromosomally integrated strains. The growth rates of wild type, Δ*pslD* and Δ*pilA* strains are nearly identical (to within measurement error), as shown in Supplementary Figure 1.

Construction of allelic exchange vectors

All plasmids and primers used in genetic manipulations are listed in Supplementary Tables 2 and 3, respectively. A deletion allele for *pilA* was assembled by removing an in-frame, 405 bp fragment of coding sequence from the *pilA* open reading frame (ORF). Briefly, two PCR products, which were amplified using primers that targeted the adjacent upstream and downstream regions of the chromosome flanking *pilA*, were joined via splicing by overlapping extension (SOE) PCR. The upstream forward and downstream reverse primers used to generate this deletion allele were tailed with *attB*1 or *attB*2 sequences as described in the Gateway Cloning Technology Manual (Invitrogen) and, using Gateway technology, the Δ*pilA* allele was

recombined with pDONR223 using BP Clonase II (Invitrogen) to create pJJH126. This plasmid was then sequenced using M13F and M13R primers. Next, the Δ*pilA* allele from pJJH126 was recombined with pEX18GmGW using LR Clonase II (Invitrogen) to create the allelic exchange vector pJJH130. The allelic exchange vectors pHL129[13] and pMA9[14], which were used to generate an in-frame deletion in *pslD* and replace the *pslA* promoter with *araC-pBAD*, respectively, were obtained from Dr. D. J. Wozniak at Ohio State University.

Construction of *P. aeruginosa* deletion mutants

Wild type *P. aeruginosa* PAO1 was obtained from the laboratory of Dr. Colin Manoil at the University of Washington. Allelic exchange vectors were introduced into *P. aeruginosa* PAO1 by standard methods for conjugation[35] and unmarked deletion mutations were constructed using established procedures for two-step allelic exchange[35]. Deletions that were constructed in *pilA* and *pslD*—which resulted in the cell lines *P. aeruginosa* JJH492 and JJH498, respectively—were confirmed by PCR using primers targeting the outside, flanking regions of the gene (Supplementary Table 3). These PCR products were then sequenced using these same primers in order to confirm precise, in-frame deletion of the target gene. Two-step allelic exchange using pMA9 to replace the *pslA* promoter with *araC*-P_{BAD} was carried out as previously described[14] and resulted in the cell line BTPA48. The site-specific insertion of *araC*-P_{BAD} was confirmed by PCR with primers targeting the outside, flanking regions of the *pslA* promoter (Supplementary Table 3), and the PCR products were then sequenced using these same primers to confirm the correct insertion.

Construction of miniTn7 Vectors

The Gateway compatible destination vector pUC18-miniTn7T2-Gm-GW was built for the purpose of making single-copy chromosomal insertions with multiple, divergently transcribed open reading frames (ORFs). To begin, a DNA fragment containing tandem T4 terminators and 5' overhangs compatible with the KpnI restriction digestion site was created *in vitro*. To do this, complementary 5'-phosphorylated ssDNA oligomers containing T4 terminator sequences (Supplementary Table 3) were combined in equimolar ratios, boiled for 15 min at 100°C and then cooled in stepwise increments of 2°C per 3 min until the mixture reached 22°C. The assembled dsDNA fragment was then ligated into the KpnI digested pUC18-miniTn7T-Gm-GW (Supplementary Table 2). Ligated plasmids were transformed into *E. coli* ccdB Survival 2™ T1R (Supplementary Table 1) and clones harboring the correct insert were identified by colony PCR using the primers JH506 and JH507 (Supplementary Table 3). The DNA sequences of the resulting plasmids were verified by Sanger sequencing using the primer JH507. The final construct, pUC18-miniTn7T2-Gm-GW, has terminator sites at both ends of the transposon to prevent read-through transcription into the *P. aeruginosa* chromosome in either direction.

Construction of fluorescently labeled strains

Multisite Gateway technology (Invitrogen) was used to build miniTn7 vectors in which a constitutive promoter was fused to an ORF encoding a fluorescent protein. Initially, the *trc* promoter was cloned from mini-CTX2[36] using primers OBT253 and OBT254 and the resulting PCR product was recombined into pDONR221 P5-P2 using BP Clonase II to generate pBT200. Next, genes encoding the fluorescent proteins mTFP1 and mCherry were cloned from pNCS-mTFP1 and pUCP18-mCherry, respectively, using primers OBT257 and OBT258 and then

recombined into pDONR221 P1-P5r using BP Clonase II, creating pBT202 and pBT218, respectively. Analogously, *eyfp* was cloned from pEX19EYFP using primers OBT258 and OBT267 and then recombined into pDONR221 P1-P5r to generate pBT210. Primer OBT258 contained a synthetic consensus ribonuclease III and ribosomal binding sites to drive the expression of the cloned ORF. All of the entry constructs were sequenced using M13F(-21) and M13R primers (Supplementary Table 3). Subsequently, the donor plasmids containing the *trc* promoter (pBT200) and the fluorescent proteins pBT202, pBT207, and pBT210 were then recombined with pUC18-miniTn7T2-Gm-GW using LR Clonase II plus to create pBT214, pBT218, and pBT221, respectively. In order to optimize fluorescence, the QuikChange Lightning Kit (Agilent Technologies) and the oligonucleotides OBT314 and OBT315 were used to introduce the constitutive A1/04/03 promoter[37] and remove the *trc* promoter from these constructs, generating pBT214, pBT218, and pBT221, respectively. Finally, *P. aeruginosa* strains were labelled with the fluorescent proteins using the miniTn7 system as previously described[38]. Here, the fluorescent strains BTPA94, BTPA98 and BTPA101 were created by inserting the miniTn7 from pBT273, pBT277, and pBT279, respectively, into the chromosome of *P. aeruginosa* JJH0 with the helper plasmid pTNS2, according to established methods for electroporation and selection[38].

Confocal micrographs

Log phase cultures grown in FAB containing 30 mM glutamate were diluted to a final OD_{600} of 0.05 in FAB containing 0.6 mM glutamate. For biofilms containing multiple strains, each strain was grown to log phase and diluted to an OD_{600} of 0.05 individually. Equal volumes of each strain were then mixed for the inoculum. Bacteria were inoculated into a flow cell and allowed to attach for 15 min before initiation of 3 ml/hr flow with fresh FAB containing 0.6 mM

glutamate. Biofilms were grown at 30°C. Cells were visualized using a Zeiss LSM 510 confocal laser scanning microscope. Image series were processed using Volocity (Improvision). For experiments with Syto9 staining, DNA was stained using the cell permeable Syto9 stain (Invitrogen) at 5 μM. The stain was incubated statically in the flow cell for 15 min before resuming flow to remove residual dye and imaging of the cells/trails.

To determine the co-localization of the HHA- and Syto9-stained areas, background-subtracted images were analyzed first for the total number of HHA-positive pixels. The Syto9-positive subset of these HHA positive pixels was then determined. The ratio of Syto9-positive and HHA-positive pixels to total HHA-positive pixels was calculated to determine the overlap between the two stains.

Computer Simulations

1. Motivation

To test the hypothesis that simple random motion biased by the presence of Psl leads to the type of exploratory behavior that is observed experimentally (and characterized by effective power-law behavior), we performed model calculations. From a statistical mechanics point of view, this is a complicated system: entities do not have an instantaneous pairwise interaction that affects their trajectories, but instead are influenced by the entire history of each other's (and their own) motion. Bacteria deposit a trail of Psl that affects any bacterium encountering it at a later point, and (unlike typical situations with time-delayed interactions) this interaction does not weaken if the time between the two visits increases. To tackle this complexity, we adopted an agent-based model in which Psl deposition and bacterial motion are accounted for separately. The pivotal questions are then whether this type of behavior (bacterial motion biased by the

entire visit history of all agents in the system) leads to the trajectories observed experimentally; and how the coupling to the visit history (i.e. rate at which Psl is deposited in earlier visits) affects these trajectories. For the *unbiased* bacterial motion, we used experimental input from the $\Delta P_{psl}/P_{BAD}$-*psl* in the absence of arabinose to calibrate the simulation. However, it is important to note that this is not sufficient: adoption of the experimental (unbiased) motion without a proper model for the role of Psl in biasing the actual bacterial displacements would lead to random-walk-like behavior (random reorientations separated by relatively straight trajectories, i.e. the behavior observed in the absence of Psl deposition).

2. Model and bacterial motion

System geometry and initial conditions. We performed simulations in which the surface motion of bacteria was modeled by non-overlapping line segments of unit length that moved in a square periodic domain of side length $L = 35$. Given the bacterium length of 1.9 μm, this corresponded to a domain of roughly 66×66 μm^2, similar to the experimental viewing window. The simulation began with 10 bacteria on the surface in a random, non-overlapping configuration and advanced from there in a series of time steps during which each bacterium could move, multiply and deposit Psl. The run length was determined by the total number of bacterium-time steps (i.e. the integrated value of the bacterial population over time), which was set to 500,000 in accordance with the experiments. The bacterium growth process proceeded stochastically, leading to a run length of 8300 ± 800 time steps. Each time step represented 3 seconds of real time, so that the simulations corresponded to an experimental run of approximately 7 hours, roughly equal to the duration of the exponential growth phase in the experiments from which most of the salient visit history is taken. To avoid artifacts that result from moving the bacteria in a prescribed order, the bacteria were chosen stochastically. For a configuration of n bacteria, a

time step corresponded to n consecutive moves, in each of which a bacterium was chosen at random.

Psl deposition. The bacterial properties in the simulations were modeled after the arabinose-inducible $\Delta P_{psl}/P_{BAD}$-*psl* mutant, which deposits Psl at a rate determined by the concentration of arabinose in solution. As such, each bacterial move started with the deposition of an amount of Psl equal to r_{Psl}, which was varied between runs to correspond with the variation of arabinose content across different experiments. The Psl accumulation was recorded at the point under the center of the bacterium, in a grid with mesh size a equal to $1/29^{th}$ of a bacterium length. The total size of this grid was approximately 10^6 bins, corresponding to the size of the pixel grid used in experiments. In the absence of arabinose, the bacteria produce no Psl, i.e. $r_{Psl} = 0$. To model non-zero concentrations of arabinose, r_{Psl} was varied from 10^{-5} (for which bacterial behavior did not vary appreciably from the simulation with $r_{Psl} = 0$) to 10^{-3} (where the effects of increasing r_{Psl} saturated).

Bacterial motion. To obtain proper bacterial behavior, we started by modeling bacterial motion in the absence of Psl. It was observed experimentally that bacterial displacements lay within a wedge emanating from the bacterium's current position. We modeled this by moving a bacterium with a step size s at an angle θ from the cell's body axis, see Supplementary Figure 12. During this move, the orientation of the director did not change. The displacement s was assigned randomly to each bacterium at birth according to the experimentally determined distribution $P_s(s)$ and remained unchanged for the duration of the simulation to model the persistent nature of bacterial speeds, whereas the deviation angle θ was chosen randomly per move according to a distribution $P_\theta(\theta)$, also obtained from experiments. To obtain these experimental distributions, arabinose-inducible bacteria were monitored in the absence of arabinose and their speeds and

deviation angles were recorded over the course of an experimental run. The functions $P_s(s)$ and $P_\theta(\theta)$ were then obtained by fitting functional forms to the displacement and deviation angle histograms (Supplementary Figures 13 and 14). To allow for bacterial reorientations originating from a variety of mechanisms[39,40], a fraction p_{reorient} of all moves consisted of a random body-axis reorientation with zero displacement. Since the mean square displacement (MSD) of a bacterium depends on this reorientation rate, we determined p_{reorient} by matching the average bacterial MSD to experimental observations, yielding $p_{\text{reorient}} = 0.037$ (Supplementary Figure 15).

Bacteria can associate with Psl. To model this, the displacement and deviation angle distributions were multiplied by a probability function

$$P_{\text{Psl}}(\rho_{\text{Psl}}(\mathbf{r})) = C^{-1}\{1 - \exp[-(\rho_{\text{Psl}}(\mathbf{r}) + \rho_0)\,]\} \qquad (1)$$

which depends on the Psl content ρ_{Psl} at the destination position $\mathbf{r}$ of the leading pole of the bacterium, and the Psl offset ρ_0. C is a normalization constant. ρ_{Psl} is obtained by sampling the local Psl environment with a square "sensor" of side length equal to the bacterium width in experiment, 0.6 μm, centered at the leading pole of the bacterium in its new configuration. ρ_{Psl} is then the sum of all Psl previously deposited inside the sensor region, which is equal to the total number of previous bacterial visits to the sensor region multiplied by the deposition rate r_{Psl}. A deposition rate as quoted is thus the product of the actual deposition rate and a multiplicative "coupling constant" representing the sensitivity of the bacterial motion to a given amount of Psl. The range of deposition rates is chosen such that an appreciable response occurs over the time scale of the simulations (which is comparable to the time window covered experimentally), without attaining saturation levels. The effect of the presence of Psl was tuned by adjusting the offset ρ_0. For $\rho_0 \to \infty$, the presence of Psl has no effect, whereas for $\rho_0 = 0$ no moves to Psl-

devoid regions will take place at all. A small value of ρ_0 is sufficient to ensure that the visit histograms in the simulations varied more than in the experiments over the range of Psl deposition rates and arabinose concentrations used (Figures 2d and 2e). We chose $\rho_0 = 0.001$.

Rather than explicitly constructing the joint distribution of $P_s(s)$, $P_\theta(\theta)$ and $P_{\mathrm{Psl}}(\rho_{\mathrm{Psl}}(\mathbf{r}))$ during each single bacterium move, we instead used a stochastic process in which either a step according to $P_s(s)$ and $P_\theta(\theta)$ or a reorientation was proposed, which then was accepted or rejected according to $P_{\mathrm{Psl}}(\rho_{\mathrm{Psl}}(\mathbf{r}))$. Upon rejection, a new move was proposed until one was accepted. To avoid deadlock situations, the number of move attempts was limited to $N_{\max}$. The resulting error was limited by choosing $N_{\max}$ large enough such that moves were aborted (resulting in a bacterium staying in place during that time step) less than 1% of the time for all deposition rates (accordingly, the choice of $N_{\max}$ depended on the Psl offset ρ_0). Excluded volume of the bacteria was incorporated in this method by rejecting any proposed move that resulted in bacterial overlap.

Bacterial growth. To model the exponential growth of bacteria, each bacterium could divide during each time step with a probability p_{growth} chosen to match the exponential population growth rate observed in the experiments (Supplementary Figure 16). The new bacterium was placed with its long axis along the director of its parent, displaced one bacterium length in front of or behind the parent with equal probability. The director of the new bacterium was either parallel or antiparallel to the director of the parent, with equal probability.

3. Sampling and data analysis

To compare directly to experimental observations, we collected the bacterial visit distribution during each run, recording bacterial visits in a square grid with the same resolution

as the experimental pixel grid ($1/29^{th}$ of a bacterium length). In each time step, bacteria were allocated to the pixel containing their center. Upon completion of the run, pixels were binned by the number of bacterial visits. To obtain good statistics at high visit numbers (which occur least frequently) we averaged over 100 independent runs for each deposition rate.

Supplementary Table 1. Bacterial strains.

Strain	Genotype, description or relevant characteristics	Source
Escherichia coli		
NEB5α	*fhuA2 Δ(argF-lacZ)U169 phoA glnV44 Φ80Δ (lacZ)*M15 *gyrA96 recA1 relA1 endA1 thi-1 hsdR17*	New England BioLabs
ccdB Survival 2™ T1R	Str^r; *F$^-$ mcrA Δ(mrr-hsdRMS-mcrBC) Φ80lacZΔM15 ΔlacX74 recA1 araΔ139 Δ(ara-leu)7697 galU galK rpsL endA1 nupG fhuA::*IS2	Invitrogen
DB3.1	Str^r; *F$^-$ gyrA462 endA1 Δ(sr1-recA) mcrB mrr hsdS20 (r_B^- m_B^-) supE44 ara-14 galK2 lacY1 proA2 rpsL20 xyl-5 Δleu mtl-1*	[38]
S17.1 (λ_{pir})	F$^-$ RP4-2-Tc::Mu *aphA*::Tn7 *recA* λpir lysogen, Sm^r, Tc^r	Lab archive[41]
SM10 (λ_{pir})	F$^-$ RP4-2-Tc::Mu *recA* λpir lysogeny, Km^r	Lab archive[41]
Pseudomonas aeruginosa		
JJH0	PAO1 wild type strain originating from the laboratory of Dr. Colin Manoil (MPAO1)	Lab Archive[42]
BTPA48	JJH0 in which the *pslA* promoter and 5' regulatory regions have been replaced with *araC* and an arabinose inducible promoter (P_{BAD})	This study[14]
BTPA94	JJH0 containing a gene encoding mTFP1 driven by a constitutive promoter integrated at the attTn7 site; Gm^r	This study
BTPA98	JJH0 containing a gene encoding mCherry driven by a constitutive promoter integrated at the attTn7 site; Gm^r	This study
BTPA101	JJH0 containing a gene encoding eYFP driven by a constitutive promoter integrated at the attTn7 site; Gm^r	This study
JJH492	JJH0 Δ*pilA*	This study
JJH498	JJH0 Δ*pslD*	This study

Km, kanamycin; Sm, streptomycin; Tc, tetracycline

Supplementary Table 2. Plasmids.

Plasmid	Description or relevant characteristics*	Source
pDONR223	Entry vector for single-fragment Gateway cloning, contains the donor *attP*1/*attP*2 recombination sites flanking *ccdB* and *cat*, Sp^r, Cm^r	43
pEX18GmGW	Allelic exchange vector with *sacB* and *oriT*, containing the Gateway (GW) destination *attR*1/*attR*2 recombination sites flanking *ccdB* and *cat*, Cm^r, Gm^r	44
pJJH126	pDONR223 with an *attL*1/*attL*2 flanked, 784 bp deletion construct for PAO1 *pilA*, Sp^r	This study
pJJH130	pEX18GmGW with an *attB*1/*attB*2 flanked, 784 bp deletion construct for PAO1 *pilA*, Gm^r	This study
pHL129	pEX18Gm derived allelic exchange vector with *sacB* and *oriT*, bearing a deletion construct for PAO1 *pslD*, Gm^r	13
pUC18-miniTn7T-Gm-GW	Cm^r, Ap^r and Gm^r; *aacC1* on mini-Tn7 based vector with a transcriptional terminator at the right end of the Tn7 transposon; Gateway compatible destination vector (AY737004)	38
pUC18-miniTn7T2-Gm-GW	Cm^r, Ap^r and Gm^r; pUC18-miniTn7T-Gm-GW containing an additional, synthetic tandem T4 terminator inserted at the kpnI site at the left end of the Tn7 transposon	This study
pTNS2	T7 transposase expression vector	38
mini-CTX2	source for $lacI^q$ and the IPTG inducible *trc* promoter; Tc^r	36
pNCS-mTFP1	source for mTFP1 (monomeric teal fluorescent protein 1); Ap^r	Allele Biotech
pUCP18-mCherry	source for mCherry; Ap^r	45
pEX19EYFP	source for eYFP; Gm^r	46
pDONR221 P1-P5r	GateWay-compatible vector with attP1 and attP5r recombination sites and *ccdB*; Kn^r and Cm^r	Invitrogen
pDONR221 P5-P2	GateWay-compatible vector with attP5 and attP2 recombination sites and *ccdB*; Kn^r and Cm^r	Invitrogen
pBT200 (pENTR-Ptrc)	A GateWay compatible plasmid containing the *trc* promoter flanked by attL2 and attL5 recombination sites; Kn^r	This study
pBT202 (pENTR-mTFP1)	A GateWay compatible plasmid containing *mtfp1* flanked by attR5 and attL1 recombination sites; Km^r	This study
pBT207 (pENTR-mCherry)	A GateWay compatible plasmid containing *mcherry* flanked by attR5 and attL1 recombination sites; Km^r	This study
pBT210 (pENTR-eYFP)	A GateWay compatible plasmid containing *eyfp* flanked by attR5 and attL1 recombination sites; Km^r	This study
pBT214 (pUC18-miniTn7T2-Ptrc-mTFP1)	miniTn7 transposon with *mtfp1* driven by the *trc* promoter; Ap^r, Gm^r	This study
pBT218 (pUC18-miniTn7T2-Ptrc-mCherry)	miniTn7 transposon with *mcherry* driven by the *trc* promoter; Ap^r, Gm^r	This study
pBT221 (pUC18-miniTn7T2-Ptrc-eYFP)	miniTn7 transposon with *eyfp* driven by the *trc* promoter; Ap^r, Gm^r	This study

pBT273 (pUC18-miniTn7T2-PA1/04/03-mTFP1)	miniTn7 transposon with *mtfp1* driven by the A1/04/03 promoter; Ap^r, Gm^r	This study
pBT277 (pUC18-miniTn7T2-PA1/04/03-mCherry)	miniTn7 transposon with *mcherry* driven by the A1/04/03 promoter; Ap^r, Gm^r	This study
pBT279 (pUC18-miniTn7T2-PA1/04/03-eYFP)	miniTn7 transposon with *eyfp* driven by the A1/04/03 promoter; Ap^r, Gm^r	This study
pMA9	pEX18Gm derived allelic exchange vector with *sacB* and *oriT*, bearing an *araC-pBAD* knock-in construct to replace the *pslA* promoter	[14]

Cm, chloramphenicol; Gm, gentamicin; Sp, spectinomycin

Supplementary Table 3. Primers.

Oligonucleotide	DNA sequence*
DNA Sequencing and verification of deletion or insertion mutations	
M13F	GTA AAA CGA CGG CCA G
M13F(-21)	TGT AAA ACG ACG GCC AGT
M13R	CAG GAA ACA GCT ATG AC
JH506	GGC CGA TTC ATT AAT GCA GC
JH507	GTG TAA AGC CTG GGG TGC
OBT282_pslAPro_outside_F	CTG AAG ATG CAG CAG CGC TG
OBT283_pslAPro_outside_R	TTG CCG CAG GCG GTG GAC
pslD_outside_F	CCG AGG TCT ACC ATT CCC ACG
pslD_outside_R	GAA CTT GGT GCG CTT CCA CAG
rjs_pilA_F	CCA AAT CGA GGA AAT CCA GCT GTC
rjs_pilA_R	GAA GCG GGG CTT TTT TAT GCG
Construction of miniTn7 vectors	
JH510_T4-Term-kpnI-1	5'phos-CTT GGG GAC CCT AGA GGT CCC CTT TTT TAT TTT TTG GGG ACC CTA GAG GTC CCC TTT TTT ATT TTG GTA C
JH511_T4-Term-kpnI-2	5'Phos-CAA AAT AAA AAA GGG GAC CTC TAG GGT CCC CAA AAA ATA AAA AAG GGG ACC TCT AGG GTC CCC AAG GTA C
OBT253	**GGGG ACA ACT TTG TAT ACA AAA GTT GCG** CTG TTT CCT GTG TGA AAT TGT TAT CCG CTC A
OBT254	**GGGG ACC ACT TTG TAC AAG AAA GCT GGG TA**T GAT AGC GCC CGG AAG AGA GTC AA
OBT257	**GGGG ACA AGT TTG TAC AAA AAA GCA GGC TCG** TCG AAT TCT TAC TTG TAC AGC TCG TCC ATG
OBT258	**GGGG ACA ACT TTT GTA TAC AAA GTT GT**A CTA TAG AGG GAC AAA CTC AAG GTC ATT CGC AAG AGT GGC CTT TAT GAT TGA CCT TCT TCC GGT TAA TAC GAC CGG GAT AAC TCC ACT TGA GAC GTG AAA AAA GAG GAG TAT TCA TGG TGA GCA AGG GCG AGG AG
OBT267	**GGGG ACA AGT TTG TAC AAA AAA GCA GGC TCG** CGC TTT ACT TGT ACA GCT CGT CCA TG
OBT314	CAG GTC GAC TCT AGA GGA TCC CCA TCA GAA AAT TTA TCA AAA AGA GTG TTG ACT TGT GAG CGG ATA ACA ATG ATA CTT AGA TTC AAT TGT GAG CGG ATA ACA ATT TCA CAC ATC TAG AAT TAA AGA GGA GAA ATT AAG CAT GGT GAG CAA GGG CGA GGA G
OBT315	CTC CTC GCC CTT GCT CAC CAT GCT TAA TTT CTC CTC TTT AAT TCT AGA TGT GTG AAA TTG TTA TCC GCT CAC AAT TGA ATC TAA GTA TCA TTG TTA TCC GCT CAC AAG TCA ACA CTC TTT TTG ATA AAT TTT CTG ATG GGG ATC CTC TAG AGT CGA CCT G

Construction of vectors containing in-frame deletion alleles

JH453_pilAupF01-GWB1	**GGG GAC AAG TTT GTA CAA AAA AGC AGG CTC** AGT CAC CAG CGA CAG CTT G
JH454_pilAupR01	*ATC ACC TTA GTT ATC ACA ACC TTT CGG* GGT AAA GCC TTT TTG AGC TTT C
JH455_pilAdownF01	CCG AAA GGT TGT GAT AAC TAA G
JH456_pilAdownR01-GWB2	**GGG GAC CAC TTT GTA CAA GAA AGC TGG GTG** GCC GAT ATC GTC ATG CTC

* Regions of homology to the target amplicons are underlined, regions of reverse complementarity are *italicized*, and Gateway *attB*1 and *attB*2 sequences are in **bold**.

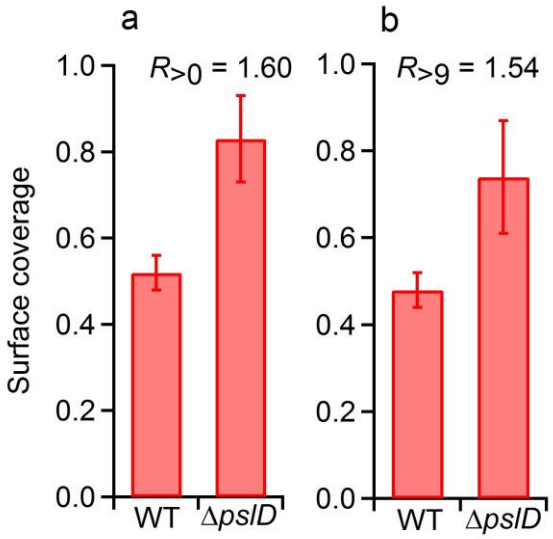

Supplementary Figure 11. Effects of short visits of bacteria on the surface coverage. **a**. Comparison between WT and Δ*pslD* at N_s = 124,000 using data from all tracked bacteria included. **b**. Comparison between WT and Δ*pslD* at N_s = 124,000 using data from bacteria with residence time t_{res} > 9 s. $R_{>0}$ and $R_{>9}$ are the surface coverage ratios of Δ*pslD* and WT using the data for bacteria residence times t_{res} > 0 s and t_{res} > 9 s, respectively. Average values（*N*=5 for WT; *N*=3 for Δ*pslD*） are presented in the histograms. Error bars represent standard error of the mean (SEM) of the measurements.

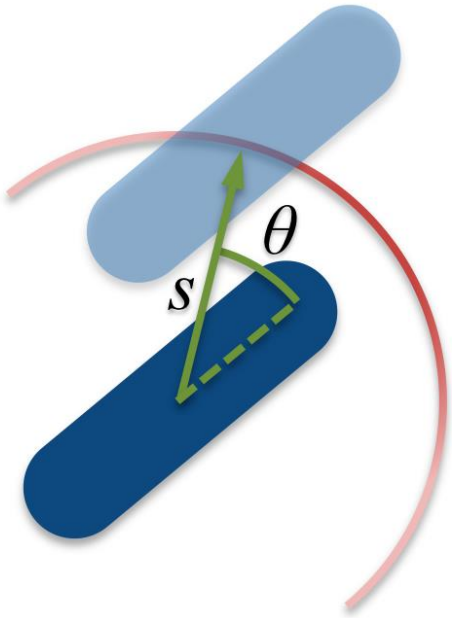

Supplementary Figure 12. Schematic of a single bacterium step in simulations. Pictured is a bacterium moving from its old position (dark spherocylinder) to a new position (light spherocylinder). The bacterium center is displaced over a distance s while maintaining director orientation. The angle deviation $-\pi/2 \leq \theta \leq \pi/2$ was chosen from a distribution that is symmetric around $\theta = 0$ (depicted by arc, variation in shading reflects variation of probability). Figure is not to scale; notably, the typical distance s is only a fraction of the bacterial length, cf. Supplementary Figure 13.

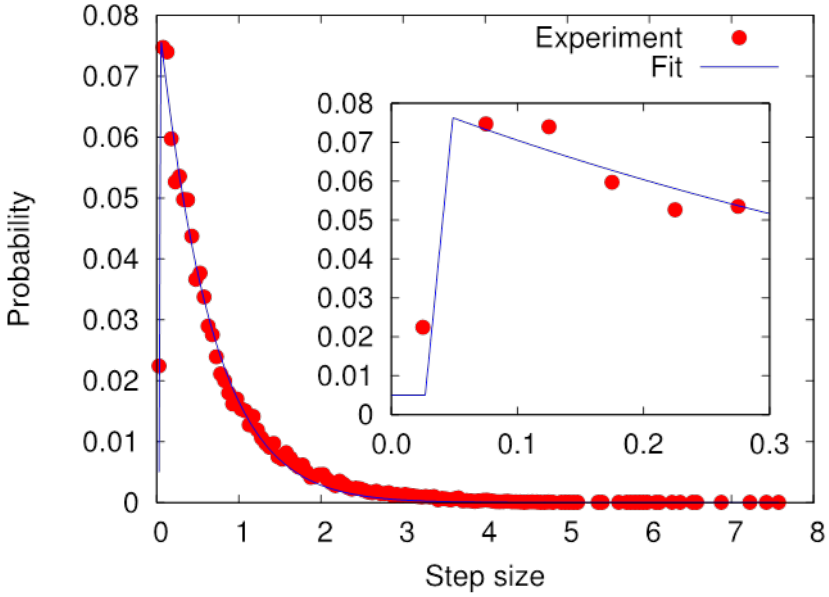

Supplementary Figure 13. Experimentally observed displacement distribution for $\Delta P_{psl}/P_{BAD}$-*psl* in the absence of arabinose along with a fitted distribution that is employed in the simulations. Units are mesh size a (equal to 1/29th of a bacterium length) per 3-second interval. For $s > 0.05$ the fit is a truncated Gaussian, $P_s(s) = D^{-1}\exp\left[-\frac{(s-10.0)^2}{2\times 2.56^2}\right]$, where D ensures that the distribution is normalized. Simple continuation of this function to $s = 0$ overestimates the number of bacteria with very low speeds, thus distorting the tail of the visit histograms in Figure 2e. For this reason, we modeled the distribution in the regime $0 \le s \le 0.05$ as a piecewise distribution, $P_s(s) = 0.005$ for $0 \le s \le 0.027$ and $P_s(s) = 3.26s - 0.083$ for $0.027 \le s \le 0.05$ (see inset). This function was chosen such that $P_s(s)$ is continuous at $s = 0.05$ and yields the same probability for a displacement in [0, 0.05) as the left-most bin in the experimental distribution.

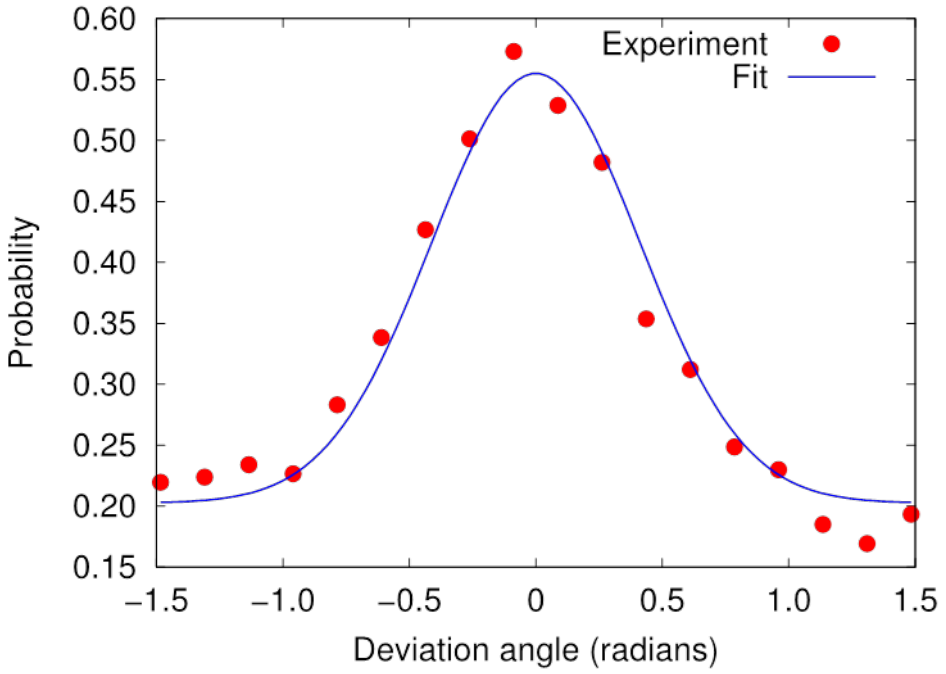

Supplementary Figure 14. Experimentally observed deviation angle distribution for $\Delta P_{psl}/P_{BAD}$-*psl* in the absence of arabinose along with the fitted distribution that was employed in the simulations. $P_\theta(\theta) = E^{-1}\left(0.202 + 0.352\exp\left[-\frac{\theta^2}{2\sigma^2}\right]\right)$, where $\sigma = 0.411$ radians and E ensures normalization. $P_\theta(\theta) = 0$ for $|\theta| > \pi/2$.

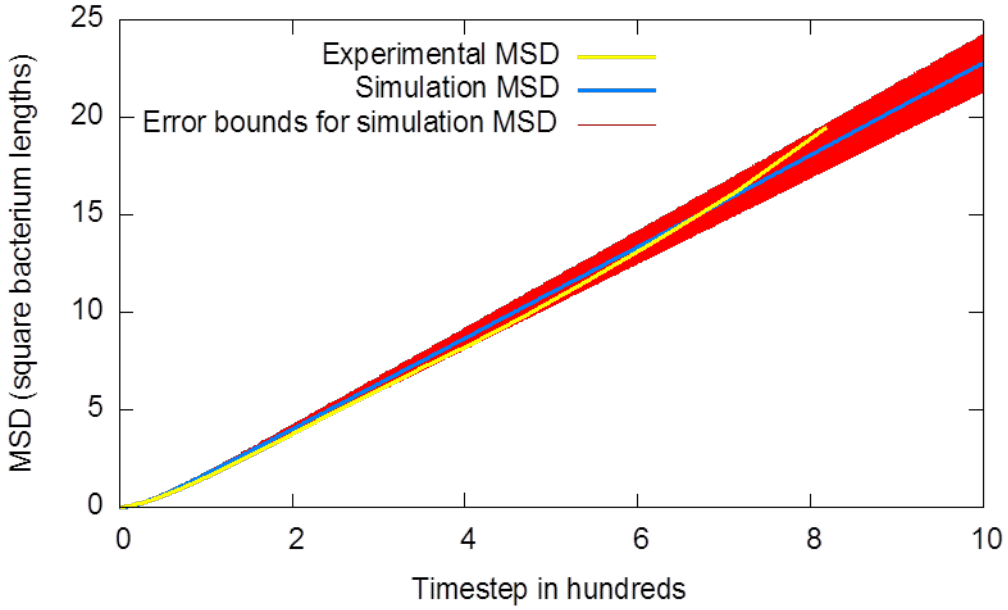

Supplementary Figure 15. Bacterial mean square displacement and corresponding simulation results. The mean square displacement in simulation depends on the probability p_{reorient} of attempting a random director reorientation. This was tuned to match the simulation data for $r_{\text{Psl}} = 0$ with experimental observations for the $\Delta P_{psl}/P_{BAD}$-*psl* mutant at 0% arabinose concentration. The simulation results were obtained from a run of 1000 bacteria monitored for 10^5 time steps each.

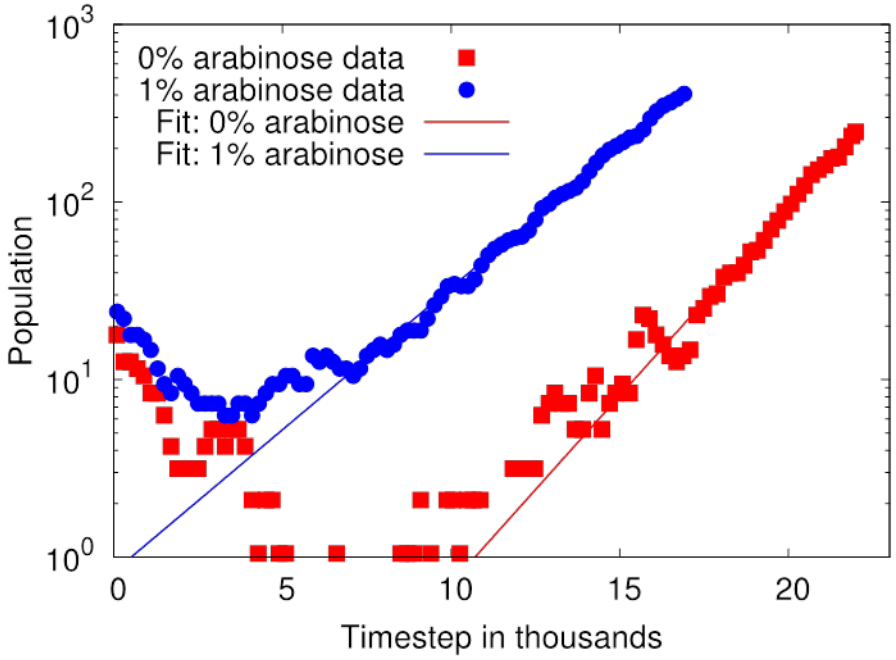

Supplementary Figure 16. Experimentally determined population size and growth rate fit. Bacterial population is shown as a function of time for the lowest and highest arabinose concentrations in experiment (0% and 1% (w/v), respectively) along with fits to the latter exponential part of the data (greater than 15,000 steps for 0% arabinose and greater than 6,000 steps for 1% arabinose). The growth rates obtained from the fits were 4.9×10^{-4} per bacterium per time step for 0% arabinose and 3.7×10^{-4} per bacterium per time step for 1% arabinose. Since the visit distributions determined in our model (Figure 2e) were not sensitive to the second significant digit of the growth rate, the average of these two rates (4.3×10^{-4} per bacterium per time step) was used for all Psl deposition rates.

Supplementary References

33. Singh, P. K., Parsek, M. R., Greenberg, E. P. & Welsh, M. J. A component of innate immunity prevents bacterial biofilm development. *Nature* 417, 552–5 (2002).

34. Vogel, H. J. & Bonner, D. M. Acetylornithinase of *Escherichia coli*: partial purification and some properties. *J Biol Chem* **218**, 97–106 (1956).

35. Hoang, T. T., Karkhoff-Schweizer, R. R., Kutchma, A. J. & Schweizer, H. P. A broad-host-range Flp-FRT recombination system for site-specific excision of chromosomally-located DNA sequences: application for isolation of unmarked *Pseudomonas aeruginosa* mutants. *Gene* **212**, 77–86 (1998).

36. Hoang, T. T., Kutchma, A. J., Becher, A. & Schweizer, H. P. Integration-proficient plasmids for *Pseudomonas aeruginosa*: site-specific integration and use for engineering of reporter and expression strains. *Plasmid* **43**, 59–72 (2000).

37. Lanzer, M. & Bujard, H. Promoters largely determine the efficiency of repressor action. *Proc Natl Acad Sci U S A* **85**, 8973–7 (1988).

38. Choi, K. H. & Schweizer, H. P. mini-Tn7 insertion in bacteria with single attTn7 sites: example *Pseudomonas aeruginosa*. *Nat Protoc* 1, 153–61 (2006).

39. Conrad, J. C. et al. Flagella and pili-mediated near-surface single-cell motility mechanisms in *P. aeruginosa*. *Biophys J* **100**, 1608–16 (2011).

40. Jin, F., Conrad, J. C., Gibiansky, M. L. & Wong, G. C. L. Bacteria use type-IV pili to slingshot on surfaces. *Proc Natl Acad Sci U S A* **108**, 12617–22 (2011).

41. Simon, R., Priefer, U. & Puhler, A. A broad host range mobilization system for in vivo genetic-engineering - transposon mutagenesis in gram-negative bacteria. *Nat Biotechnol* **1**, 784–91 (1983).

42. Jacobs, M. A. et al. Comprehensive transposon mutant library of *Pseudomonas aeruginosa*. *Proc Natl Acad Sci U S A* **100**, 14339-44 (2003).

43. Rual, J. F. et al. Human ORFeome version 1.1: a platform for reverse proteomics. *Genome Res* **14**, 2128–35 (2004).

44. Wolfgang, M. C., Lee, V. T., Gilmore, M. E. & Lory, S. Coordinate regulation of bacterial virulence genes by a novel adenylate cyclase-dependent signaling pathway. *Dev Cell* **4**, 253–63 (2003).

45. Irie, Y. *et al*. Self-produced exopolysaccharide is a signal that stimulates biofilm formation in *Pseudomonas aeruginosa*. *Proc Natl Acad Sci U S A* **109**, 20632–6(2012).

46. Guvener, Z. T., Tifrea, D. F. & Harwood, C. S. Two different *Pseudomonas aeruginosa* chemosensory signal transduction complexes localize to cell poles and form and remould in stationary phase. *Mol Microbiol* **61**, 106–18 (2006).